Diamonds for Sensing Applications

Performed on 16.04. – 19.04.2018

Authors:

F. Bayer

Y. Taege

Tutors:

J.-P. Schröder

U. Warring

Abstract

In this applied lab experiment, the principles of optically detected magnetic resonance (ODMR) of nitrogen-vacancies (NV^-) in diamonds have been investigated. Therefore, an experimental setup, including parts for optical spectroscopy, imaging and microwave-based excitation, has been improved and calibrated. After implementing reliable processing methods, the results of the calibrations were used to perform microscopy, spectral analysis and ODMR experiments on two diamonds. The size of the diamonds was determined to be in the range of $(15 \pm 12)\,\mu m$ and $(20 \pm 11)\,\mu m$, respectively. We were further able to identify the zero phonon line at $(643 \pm 2)\,nm$ in the fluorescence spectra, identifying the NV^- centers. During the ODMR experiments, the degenerated resonance of the triplet state without an applied, external magnetic field has been determined to be at $(2.86 \pm 0.02)\,GHz$, which is inline with the previous results. The spatial dependence on an external applied magnetic field has also been observed, yielding up to four symmetric resonances. Hence, we were able to show that all four possible orientations of NV^- centers were present in the observed diamonds.

With the submission of this report the authors hereby confirm that the elaboration has been made unaffiliated and that all means and sources have been quoted. Furthermore, the *Proposals for Safeguarding Good Scientific Practice* of the DFG have been taken into account.

Contents

1. Introduction and Motivation

For centuries diamonds have been a desired possession as they shine with a attracting beauty in different colors. But especially throughout the recent years, they moved into focus as they rise promise for novel applications in nanotechnology and life-science [1, 2, 3].

Special attention is paid on the nitrogen vacancy (NV) center in diamonds, which constitutes a specific defect in the diamond. Recent studies have advocated the use synthetically manufactured diamonds for the detection of magnetic fields [4]. This is particularly advantageous since they could be used as nanoscale sensors in physics, biology and medicine.

The present lab report reflects on an experiment, in which the spectral characteristics of NV centers in micro sized diamonds have been investigated. This involved the microscopy of the diamonds, the measurement of their fluorescence spectra and the detection of optically detected magnetic resonances (ODMR) [5].

The ultimate goal of this experiment is to optically detect the magnetic resonances of negatively charged NV centers (NV$^-$ centers) in diamonds. To do so, a single diamond needs to be isolated as a first step. Secondly, evidence for the existence of NV$^-$ centers needs to be proven. Thirdly, the diamonds need to be excited by microwave within a specific range in the order of GHz. To be able to achieve that, a sophisticated setup, which consists of a microscope for imaging and spectral analysis, as well as high-frequency electronic components for microwave distribution, needs to be carefully calibrated. Afterwards, the simultaneous acquisition of the diamond's fluorescence while sweeping through the desired frequency range needs to be performed.

Whereas Section 2 of this report introduces the physical concepts, necessary to follow the work, Section 3 describes how we acquired, calibrated, analyzed and optimized our measurements. The results have been summarized in Section 4 and discussed in great detail in Section 5.

2. Physical Concepts

2.1. NV Centers in Diamonds

The diamond cubic structure forms a periodic pattern of eight atoms. It can be seen as the sum of two fcc-lattices, seperated by $\frac{1}{4}$ of the width of a unit cell [6]. The NV center describes a defect, where one carbon atom is replaced by a nitrogen atom and an adjacent vacant lattice site. Thus, the symmetry axis of the defect can be oriented along eight directions (Figure 2.1), that are in principal equally populated [4].

Apart from the direction of the defect, the NV center can exist in two charge states, namely the neutral NV^0 state and the negatively charged NV^- state. Since in this experiment we investigate the properties of the negatively charged state only, it will be denoted as NV in this work.
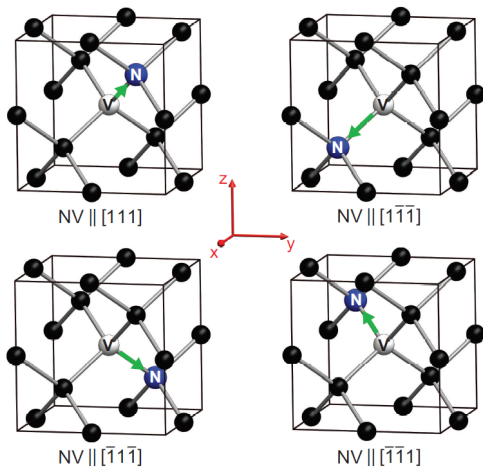
Figure 2.1: Lattice structure of diamonds with four different orientations of the NV centers. Black points mark carbon atoms, whereas the nitrogen atoms are marked in blue and white respectively. By reversing the position of nitrogen and the vacancy, four additional orientations can realized which are not shown in this figure. Taken from [3].
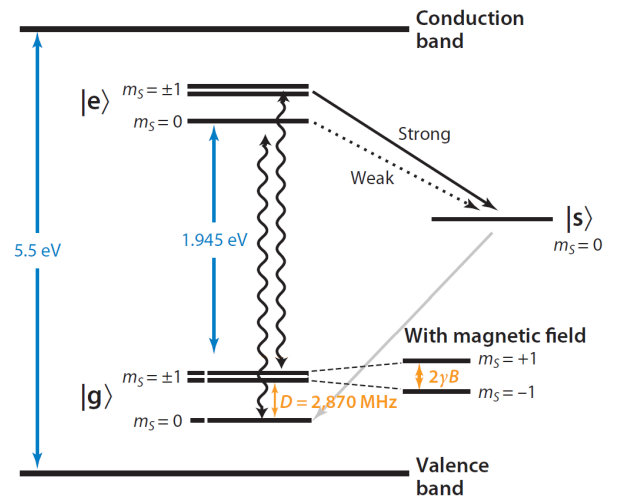
Figure 2.2: Energy-level diagram of the NV^- centers. $|g\rangle$ denotes the electronic ground state, $|e\rangle$ the electronic excited state, and $|s\rangle$ sums up metastable singlet states. Without an external magnetic field, $|g\rangle$ and $|e\rangle$ correspond to degenerated triplet states. In presence of an external magnetic field along the orientation, the $m_s = \pm 1$ states split according to the ZEEMAN effect. Adapted from [4].

2.2. Optical Properties of NV-Centers

The properties of the NV centers are mostly due to physical effects by the magnetic moment. Figure 2.2 shows the quantum states of the NV centers. The simplified quantum structure of the NV center is constructed of the ground state $|g\rangle$, the excited state $|e\rangle$ and two further states which can be seen as one metastable singlet state $|s\rangle$. The main radiative connection between the ground state and the excited state is due to the zero phonon line (ZPL). For the negatively charged NV$^-$ center, this transition contributes to a wavelength of $\lambda_{ZPL} = 637\,\text{nm}$ and has a lifetime of 10-30 ns [2]. In addition to the ZPL, photons are emitted in vibrational side bands, which in fact represents the majority of the transitions. To observe the ZPL, it is sufficient to resonate with a lower laser wavelength (in our setup $\lambda_{ex} = 519\,\text{nm}$).

In addition to the decay to the ground state $|g\rangle$, the excited state $|e\rangle$ can also emit non-radiative into the metastable singlet state $|s\rangle$. This can either occur from the state $|e, m_s = 0\rangle$, which is a weak non-radiative decay, or the state $|e, m_s = \pm 1\rangle$, which is a strong non-radiative decay.

2.3. Optically Detected Magnetic Resonance (ODMR) - Measurements

This property can be used in order to achieve a temporary decrease in optical intensity. Therefore electrons in the ground state $|g\rangle$ can be excited under the application of a microwave signal. This signal has to meet the energy difference between the states $|g, m_s = 0\rangle$ and the $|g, m_s = \pm 1\rangle$. Assuming a HAMILTONIAN $\mathcal{H}_g$, and $\mathcal{H}_s$ for the respective states, the energy difference

$$E_d = \mathcal{H}_g |g\rangle - \mathcal{H}_s |s\rangle \tag{1}$$

needs to be overcome in order to excite electrons from $|s\rangle$ to $|g\rangle$. In terms of microwave frequencies, this corresponds to [3]

$$D = \frac{E_d}{\hbar} = 2\pi \cdot 2870\,\text{MHz} \tag{2}$$

for NV$^-$ centers. Due to the strong non-radiative decay of $|g\rangle$, applying a microwave signal in the absence of a magnetic field at $f = 2870\,\text{Hz}$, the electrons will be more likely to decay non-radiatively via the metastable singlet state, leading into a decrease in intensity. This decrease can be optically detected.

In presence of a magnetic field $\vec{B}$, an additional term H_B is added onto the HAMILTONIAN [4, adapted from Eq. (1)]

$$H_B = -\vec{\mu} \cdot \vec{B} \tag{3}$$

where $\vec{\mu}$ is the magnetic moment [6, pp. 745ff]

$$\vec{\mu} = \frac{\mu_B}{\hbar} \cdot g_s \cdot \vec{s} \tag{4}$$

$$= \gamma \vec{s} \tag{5}$$

with μ_B being BOHR's magneton, the g-factor $g_s \approx 2$ and the spin $\vec{s}$. γ denotes the gyromagnetic ratio, which is $\gamma = 2\pi \cdot 28.025\,\text{GHz}\,\text{T}^{-1}$ [6, p. 745] for free electrons. Thus, a magnetic field amplitude $|\vec{B}| = B_0 \neq 0$, the previously degenerated state $|g, m_s = \pm 1\rangle$ splits according to the Zeemann effect:

$$E\,|g, m_s \pm 1\rangle = (\mathcal{H} + H_B)\,|g, m_s \pm 1\rangle \tag{6}$$

$$= \mathcal{H}\,|g, m_s \pm 1\rangle + H_B\,|g, m_s \pm 1\rangle \tag{7}$$

$$= E_0 - m_s \cdot \hbar\gamma B_0 \cdot \cos\alpha \tag{8}$$

where α is the angle between the magnetic field and magnetic moment. The energy difference between the split state ΔE is then

$$\Delta E = E(m_s = 1) - E(m_s = -1) \tag{9}$$

$$= \hbar\Delta m_s \cdot \gamma B_0 \cdot \cos\alpha \tag{10}$$

$$= 2 \cdot \hbar\gamma B_0 \cdot \cos\alpha \tag{11}$$

As a result, the original resonance is split symmetrically into two magnetic ones, which are detuned around the center frequency by

$$\omega = \frac{\Delta E}{2\hbar} \tag{12}$$

$$= \gamma B_0 \cdot \cos\alpha. \tag{13}$$

Since the effect of this magnetic resonance can be optically detected, this experiment is replied to as optically detected magnetic resonance. Due to the angle α, it is not only sensitive to the amplitude of the magnetic field, but also to the orientation between the crystal and the external field. Furthermore, the isolation of the NV center intrinsic influences includes stability of this measurement, providing a sensitive tool to detect magnetic fields.

In fact, in order to optimized the sensitivity, specific microwave pulse sequences can be applied, which are inspired by the work of common nuclear magnetic resonance sequences. However, it is also sufficient to apply an electromagnetic wave with a constant amplitude to the diamonds in order to detect the ODMR signal.

Orientation of the Crystal in the laboratory frame: The resonances ω_i obtained in each direction $i = x, y, z$ correspond to an by the NV$^-$ center experienced magnetic field B_i – therefore, the relation

$$B_i = \frac{\omega_i}{\gamma} \tag{14}$$

$$= B_0 \cdot \cos\alpha_i \tag{15}$$

holds, where α_i the angle between the center's orientation $\vec{d}$ in direction i. Having a magnetic field $\vec{B}_j^{\text{ext}} = B_0 \cdot \vec{e}_j$ $(j = x, y, z)$ in the laboratory frame, we can further express the angle between those two as

$$\cos\alpha_i = \frac{\vec{B}_j^{\text{ext}} \cdot \vec{d}}{\underbrace{|\vec{B}_j^{\text{ext}}|}_{=B_0} \cdot |\vec{d}|} \tag{16}$$

$$= \frac{\sum_j B_0 \cdot d_i \cdot \delta_{ij}}{B_0 \cdot |\vec{d}|} \tag{17}$$

$$= \frac{d_i}{|\vec{d}|} \tag{18}$$

where the coordinate system corresponds to the laboratory frame, yielding

$$\boxed{\frac{B_i}{B_0} = \frac{d_i}{|\vec{d}|}} \tag{19}$$

which also follows

$$\sum_{i=1}^{3} \frac{B_i^2}{B_0^2} = \sum_{i=1}^{3} \frac{d_i^2}{|\vec{d}|^2} = 1. \tag{20}$$

This relation shows that one is able to calculate the respective ratio B_i/B_0 for up to 4 observable resonances for each direction and determine the normalized direction $d_i/|\vec{d}|$ for each orientation in the laboratory frame, under the restriction of Equation 20.

3. Experiment

3.1. Setup

To be able to achieve the experiment's objectives, the setup must fulfil two requirements: on the one hand, one needs a reliable optical system to image the diamonds onto devices for spectral, spatial and power sensitive analysis. On the other hand, a reliable radio-frequency system must be deployed, ensuring the microwave-based excitation of the diamonds magnetic resonance. Finally, both parts need to be synchronized to achieve simultaneous optical analysis while sweeping through the desired RF-range in a time-efficient manner. The way both of these parts are connected is described in the upcoming sections. A full list of the devices and elements used can be found in Table A.1 in the appendix.

### 3.1.1. Confocal Microscope

For imaging, a confocal microscope has been deployed. As shown in the lower part of Figure 3.1, two lenses (f_1 and f_2) are set up such that their focal points coincide. The object and image plane are $f_1 = 10\,\text{mm}$ and $f_2 = 80\,\text{mm}$ away from the respective lenses, forming a **4f-system**. A major advantage of this system is that only objects in the focal plane are imaged efficiently – stray light is therefore naturally suppressed, increasing the signal to noise ratio.

In the object plane, a **microstrip** (MS) is placed, on which the diamond powder is supplied. For ODMR measurements, a magnet holder is available. Illumination and excitation are achieved using a **lase**r with a wavelength $\lambda = 519\,\text{nm}$, which is directed through an optical fiber and focussed using a condensor lens. An adjustable mirror (not shown) provides another degree of freedom for adjustment.

In the further course, the diamond can be simultaneously imaged on the optical devices. For power sensitive analysis, an **avalanche photo diode** (APD) was used, providing fast response times and high sensitivity to changes. To ensure that most of the optical power reaches the APD, and that one is still able to perform spectroscopy and imaging at the same time, a **dichroic mirror** (DC$_1$) with a ratio of 90:10 (APD:System) is used. Another dichroic mirror (DC$_2$) splits the beam with a ratio of 50:50 onto a **CCD** (spatial analysis) and an **optical spectrometer** (spectral analysis). Both the CCD and spectrometer are controlled using a computer.

To ensure that no scattered laser light, which bears several magnitudes of power more than the flourescence, frequency low-pass filters (**color filters**, CF) are used to suppress this source of noise, which can be removed for alignment purposes.
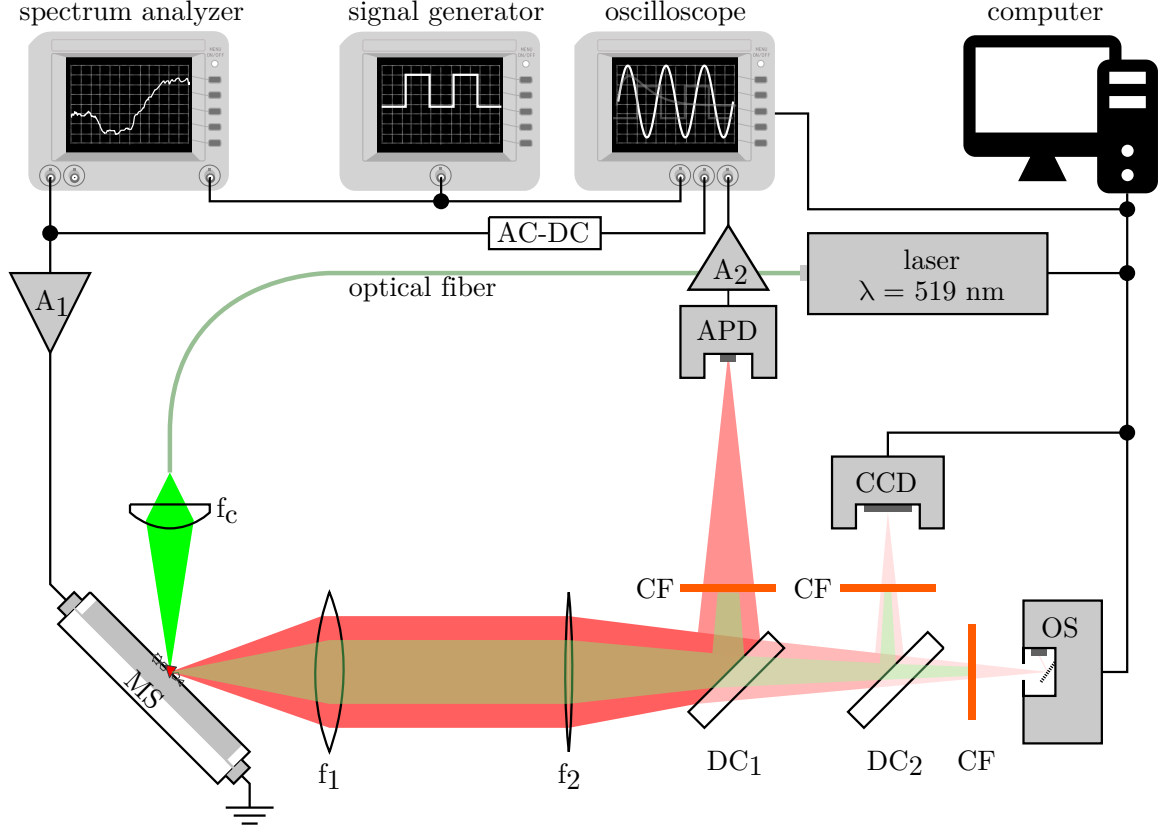
Figure 3.1: Schematic of the setup used in the experiment. The laser, controlled by driver software on a computer, is coupled into an optical fiber. **Optical setup:** Using a **condensor lens** (f_c), the laser is focussed on a microstrip (**MS**), on which diamond powder has previously been distributed. Using a 4-f-system with the lenses f_1 and f_2 (having focal lengths of 10 and 80 mm, respectively), the diamonds are imaged on an avalanche photo diode (**APD**), the CCD-camera (**CCD**) and the optical spectrometer (**OS**). Beam splitting is performed using dichroic mirrors, which split the intensities 10:90 (DC_1, beampath:APD), and 50:50 (CCD:OS). A color filters (**CF**, low pass) prevent scattered laser light from passing. **Electronic setup:** The output of a spectrum analyzer is amplified (amplifier A_1, gain = 48) and coupled into the microstrip, which is grounded through an impedance of $50\,\Omega$. The spectrum analyzer's output is simultaneously triggered with the acquisition by an oscilloscope, recording the signal of an power detector (**ACDC**), as well as the amplified signal (audio amplifier A_2) of the APD. The data feed of the oscilloscope is also connected with the computer for data acquisition. Adapted from [7].

3.1.2. Electronic Setup

Between the described microscope and the supply of microwaves, two connecting elements exist: the APD will be the detecting unit, providing quantitative information about the change in fluorescence intensity through an **oscilloscope**. The induced optical contrast for ODMR experiments will be achieved by the microstrip, which will serve as a coupler between the electronic microwave components and the diamonds. To do so, a supply covering the frequency range from approximately 2.7 to 3 GHz is necessary, which can be provided by the **tracking generator** of a **spectrum analyzer** (SA).

To start generation and acquisition simultaneously, a **signal generator** (SG) provides a trigger signal for both the SA and the oscilloscope. As the tracking generator can sweep through the aforementioned range within 200 ms, the signal generator was set to two hertz, allowing one acquisition per second. This way, a decent data-throughput is achieved, ensuring the possibility for statistical analysis of the APD's signal.

For further contrast enhancement, a strong microwave signal, which cannot be provided solely by the SA, an amplifier (A_1, gain = 48 dB) increases the power of microwaves coupled into the MS. Hence, only very few electrons will remain in the bright state. Another way to increase the obtained signal is done on the acquisition site: an audio amplifier (A_2) also increases the signal provided by the APD, which has previously been filtered using a low pass filter (cut-off frequency $f_c = 100$ Hz). The final acquisition by the oscilloscope is controlled by in-house written software[1], recording the SA's trigger and the optical signal provided by the APD. With the knowledge about the SA's sweep time and frequency range, one can calibrate the oscilloscope's time axis to frequency.

As during the course of the experiment this method revealed poor reliability, a **power detector** (AC-DC) has been included on the generation site as an improvement. To ensure that very few reflections are passed through the system, an adequate power splitter is used to connect the power detector. The provided DC-signal is then used for frequency reconstruction, which is described in Section 3.4.1.

3.2. Acquisition

The measurement of the spectral characteristics of different micro-sized diamonds has been conducted in three separate steps, which will be described in the following sections. Firstly, the microstrip has been imaged in order to choose a diamond. The desired diamond should be visible with and without the optional low pass filter, and should be isolated from other diamonds.

---

[1]https://github.com/japhsc/PyVisaRIGOL

This preliminary step has been followed by the acquisition of the fluorescence spectrum and the ODMR measurement.

3.2.1. Microscopy of the Diamonds

All optical measurements have been conducted using the microstrip as a sample holder, which is powdered with the micro-sized diamonds. However, in the interest of consistent lattice orientations, it has been desired to measure the spectra of single diamonds only. To do so, the focus of the laser has been adjusted, such that single diamonds could be illuminated. Further, the focus was pointed on a single diamond that was spatially separated from surrounding diamonds.

The CCD is used to visualize the diamonds and the adjustments of the laser beam. Due to the low pass filter, only the fluorescent light was recorded by the CCD. This has been essential to visualize the diamonds, since the bright laser light would have been dominating the light of the diamonds.

3.2.2. Identification of NV-Centers by Fluorescence

The fluorescence spectrum of the selected diamonds has been recorded with the OS in order to identify the zero phonon line of the negatively charged NV^- centre. As described in the previous section for the CCD, the laser light was filtered before reaching the OS using a low pass filter. By adjusting focus and position of the beam on the diamond, as well as the focus of the microscope, the fluorescent spectrum has been optimized to maximal intensity.

As described in Section 2.1, the NV centres can exist within the two charge states NV^0 and NV^-. To identify the desired NV^- state, the peak of the zero phonon line has been analysed. In principle, the identification can also be investigated by eye since the NV^- diamonds emit red light when excited with green light. However, the OS's spectrum has been used in this manner since it allowed to quantify our proposition.

3.2.3. ODMR-Measurements

In the last part of our measurements, the diamonds have been exposed simultaneously to laser light and a microwave signal. Throughout this measurement, the setup described in Section 3.1 has been used. Using the tracking generator of the the SA, the frequency has been centered at $2.85\,\mathrm{GHz}$ with a span of $300\,\mathrm{MHz}$.

Firstly, we used the pulsed laser mode ($f_{\mathrm{rep}} = 5\,\mathrm{Hz}$) in order to optimize the fluorescence signal on the APD. Here, the laser focus, coupling mirror and DC mirrors have provided the respective degrees of freedom.

Secondly, the laser has again been set to cw mode and the actual ODMR experiments were performed without an external magnetic field. However, it is important to notice that the earth's magnetic field (48 µT in total, 20 µT horizontally and 44 µT vertically in central Europe [8]) has also an influence on our experiment when performing the sensitive ODMR measurement. In this step, we tried to further optimize the signal with the aforementioned degrees of freedom. This process yielded a very small enhancement, though. After optimization, we acquired the same signal 200 times in order to be able to perform a statistical analysis on the signal's error and to increase the signal-to-noise ratio (SNR).

Thirdly, measurements were performed using an external magnetic field. In order to introduce a small magnetic field into the ODMR measurement, small cylindrical magnets (material: NdFeB, 6 mm in ⌀ and 13 mm in height) were used. With the use of a plastic jig, measurements with a reproducible distance of the magnets could be achieved. Five different positions of the magnets (left, right, front, back and upside) have been investigated.

To prevent the measured signal of the APD from being disturbed by the microwave signal, a Faraday cage has been designed. This has been achieved by wrapping the APD into a fine, grounded metal lattice.

After performing the ODMR experiments with the APD, we also investigated whether the CCD can be an adequate detector for measuring the decrease in contrast. A more detailed description can be found in Section 3.4.3.
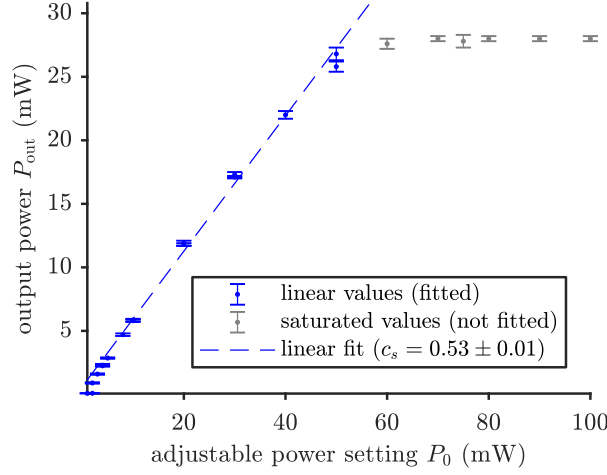
3.3. Calibration

As described in the previous section, the setup features various commercial components (such as the optical spectrometer and the SA), as well as in-house built acquisition components (e.g. the oscilloscope-SA combination and RF-components). Particularly the latter are subject to attenuation, cross talk and other factors influencing the noise and uncertainty levels, and thus need to be calibrated. This does not only insure the minimization of those uncertainties, but also allows revalidation of the acquired data.

If not stated otherwise, all errors have been calculated using the GAUSSIAN uncertainty evolution principles [9, pp. 760ff] and are denoted as VALUE ± STANDARD ERROR.

3.3.1. Coupling Efficiency of the Laser

Although the laser's driver software (IBEAM SMART, Version 1.3.0.106, TOPTICA Photonics AG, Munich, Germany) provided a GUI with adjustable power settings P_0, the actual power on the microstrip P_{out} differed from P_0. This could be due to the software not being well calibrated, but more importantly due to the fiber optics and lense, which are previously connected. To

Figure 3.2: Results of the of the adjustable power setting calibration of the driver software P_0 versus the optical output power at 519 nm at the microstrip P_out. Shown are the obtained calibration data, analyzed using weighted linear least squares fitting, resulting into $P_\text{out} = (0.53 \pm 0.01) \cdot P_0 + (0.7 \pm 0.4)$ mW. Saturated values (grey) have not been fitted, while the linear relation (blue) is included. The error bars denote the manually determined uncertainty due to fluctuations of the power, as observed on the power meter.

obtain the coupling efficiency c_L, which follows the relation

$$P_\text{MS} = c_L \cdot P_0 + P_\text{off} \tag{21}$$

we obtained values for the relation $P_\text{MS}(P_0)$ using a power meter, adjusted to the 519 nm line of the laser. The power meter has been placed at the position of the microstrip (refer to Figure 3.1).

The results of the calibration are shown in Figure 3.2. As one can see, the relation between P_0 and P_out is linear up to a saturation power at $P_0 \approx 55$ mW (blue dots) of $P_\text{out}^\text{sat} = (27.9 \pm 0.2)$ mW, which was calculated by taking the mean value of saturated values (denoted by grey dots) and the standard error as an uncertainty. Using a linear-least squares fitting algorithm with the relative errors as weights, we obtained a coupling efficiency of $c_L = 0.53 \pm 0.01$. All further measurements were performed either at an output power setting of $P_0 = 40$ mW, resulting in an applied power of $P_\text{out} = (21.1 \pm 0.5)$ mW, or at saturation power.

3.3.2. Optical Spectrometer

The optical calibration was performed to investigate the calibration of three points: firstly the absolute stability, i.e. whether the known absorption lines of a spectrum correspond to the ones measured. Secondly, the relative stability, i.e. whether the difference between two lines in the spectrum is correct. And, thirdly, the angle-stability, i.e. whether the incoupling angle

influences the acquired spectrometer.

Absolute stability: We acquired a spectrum of the surrounding sunlight through the window's glass from all directions, and used manually identified absorption lines for the absolute calibration, as shown in Figure 3.3. The lines taken from [10, p. 175], as well as the measured ones, are provided in Table 3.1. We noted a mean offset $\lambda_{\text{off}} = (-1.3 \pm 0.3)\,\text{nm}$, which will be subtracted in further measurements.
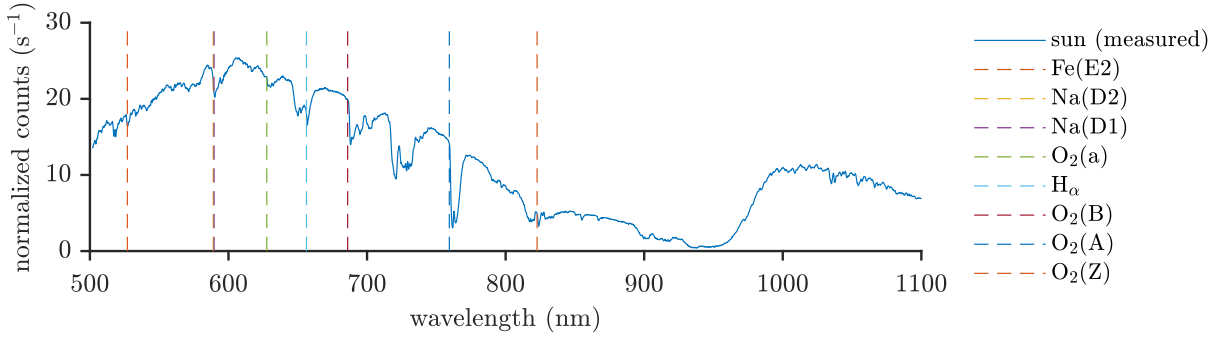
Figure 3.3: Optical spectrum of the sun, obtained from all directions through the lab's glass window. Manually identified absorption lines are denoted by horizontal lines, which can be looked up in Table 3.1. The normalized intensity reported by the spectrometer was normalized by the acquisition time.

Table 3.1: Results of the absolute calibration of the optical spectrometer. Literature values are taken from [10, p. 175], while measured values are manually taken from the minima of the obtained sun spectrum. The mean difference is $(-1.3 \pm 0.3)\,\text{nm}$.

line	Fe(E2)	Na(D2)	Na(D1)	$O_2(a)$	H_α	$O_2(B)$	$O_2(A)$	$O_2(Z)$
literature (nm)	527.0	589.0	589.6	627.7	656.3	686.0	759.4	822.7
measured (nm)	527.2	590.1	592.0	628.3	657.0	688.1	761.8	823.8
difference (nm)	-0.2	-1.1	-2.4	-0.6	-0.7	-2.1	-2.4	-1.1

Relative stability: Since a frequency-doubled laser has been used, we were able to check the calibration of the relative stability by investigating the main laser mode at $1038\,\text{nm}$, and comparing it to the position of the frequency-doubled mode. Thus, the expected ratios of λ_0 to λ_{fd} is $\frac{1}{2}$. To identify the peak position, Lorentzian and Gaussian functions were fitted to the data, which is shown in Figure 3.4 on top and bottom respectively. Since the Lorentzian function represents the peaks in a better way, it was used to analyse the peaks, resulting in $\lambda_1 = (517 \pm 2)\,\text{nm}$ and $\lambda_2 = (1033 \pm 3)\,\text{nm}$. This reveals a ratio of 0.501 ± 0.001, which is in-

line with our assumption within the uncertainties. The error was taken as the half width at half maximum (HWHM).
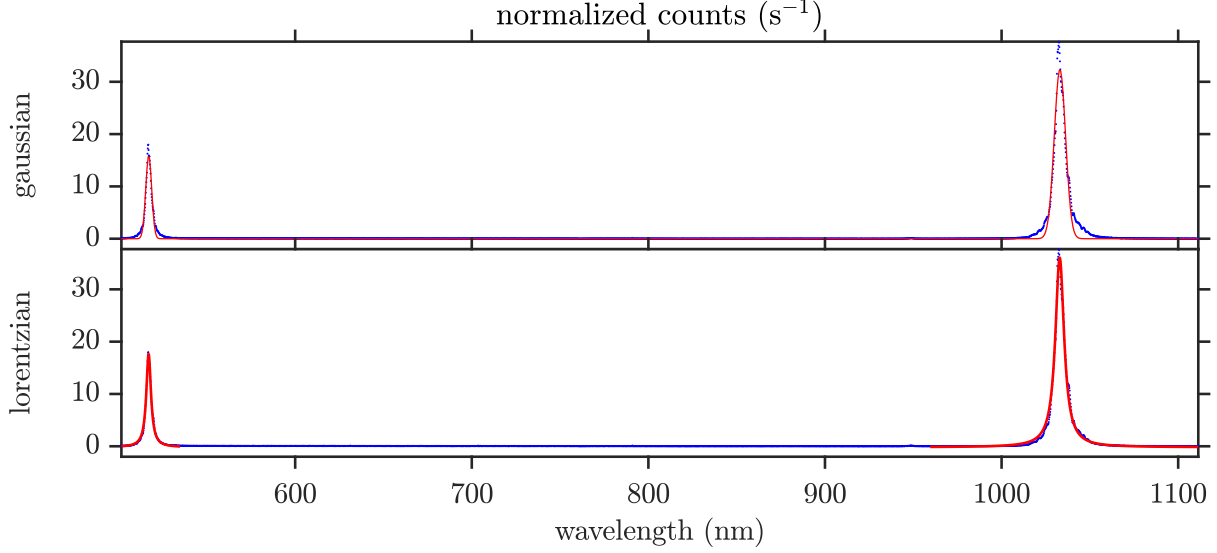
Figure 3.4: Optical spectrum of the laser the frequency doubled signal (blue) with fit Gaussian (top) and Lorentzian (bottom) functions (red).

Angle stability: The angle dependency of the spectrometer and the incident beam has been investigated in order to incorporate possible variations of the angle. For this purpose, the base-frequency's and frequency-doubled laser peaks were measured under three different angles. As in the analysis of the relative stability, the position of the peaks was determined by Lorentzian fits, resulting in Table 3.2.

As a preliminary conclusion, we would like to state that the very detailed calibration process of the spectrometer might not be of utter importance for the further course of the experiment. While the calibration offset and the angle influence the spectrum by offsets of 4 nm, the main purpose – identifying the zero-phonon-line of the NV$^-$ center – can be achieved with these uncertainties. For a proper investigation of the fluorescence, a more sophisticated spectral setup should be used.

3.3.3. Microscope

Since the ratio of the lenses used for the confocal 4f-setup is equal to the magnification $M_T = f_2/f_1$ [11], the theoretical magnification is 8. Together with the dimensions of the CCD (width

Table 3.2: Wavelength of the full and half laser peaks measured under different angles. The values were calculated with Lorentzian fits and the errors have been taken from the HWHM. The adjusted laser-wavelengths were 519 nm (half) and 1038 nm (full).

angle	half-wavelength peak (nm)	full wavelength peak (nm)
$0°$	517 ± 2	1033 ± 3
$+5°$	519 ± 1	1033 ± 4
$-5°$	516 ± 2	1034 ± 3

$w_=6.6$ mm, 1280x1024 pixels [12]), the width of one pixel d_p should correspond to

$$d_p = \frac{w}{1280} = 5.16\,\mu m \tag{22}$$

The conversion factor $c_M = [\text{pixel/m}]$ should therefore correspond to

$$c_M = \frac{1\,\text{pixel} \cdot M_T}{d_p} = 1552\,\text{pixel/mm} \tag{23}$$

To verify this assumption, the width of the microstrip $d_{MS} = (1.00 \pm 0.25)$ mm was determined using a ruler, where the uncertainties reflect half of the ruler scale (0.5 mm). The microstrip was then imaged on the CCD. As expected, the MS exceeded the sensors dimension, which is why two images with the same reference center (namely, a bright diamond which was tracked) were acquired for the calibration. In the following, we used two ways to determine whether the theoretical and observed distances agree: during acquisition, we used the measuring tool of Thorlab's software to measure the width of the microstrip. By adding the distances from upper and lower edge to a reference diamond in the centre, the total width between the edges has been determined (Figure 3.5a). As a posthoc analysis, we manually coregistered the images using GIMP (version 2.8.6, [13]) with a diamond as a reference point (Figure 3.5b). With the measurement tool of INKSCAPE (version 0.92, [14]), the distances between the upper and lower edge, as well as the uncertainties, were determined.

As denoted in Table 3.3, the obtained values are in good agreement with our theoretical considerations. Due to the incident angle of the laser beam, the upper edge is only poorly imaged: due to the way the optics are set up, the incidence is not perpendicular, resulting in a shadow. Furthermore, an object in the range of a millimeter should not be considered as a decent calibration tool – a known micrometer scale would serve better here. Since this calibration is only a proof of concept though, we can assume that the considerations are correct. Therefore, the conversion factor c_M can be used further on – other errors influencing the width of an imaged object are from higher importance, which will be discussed later on.

a) Calibration using Thorlab's software   **b)** Calibration using Coregistration
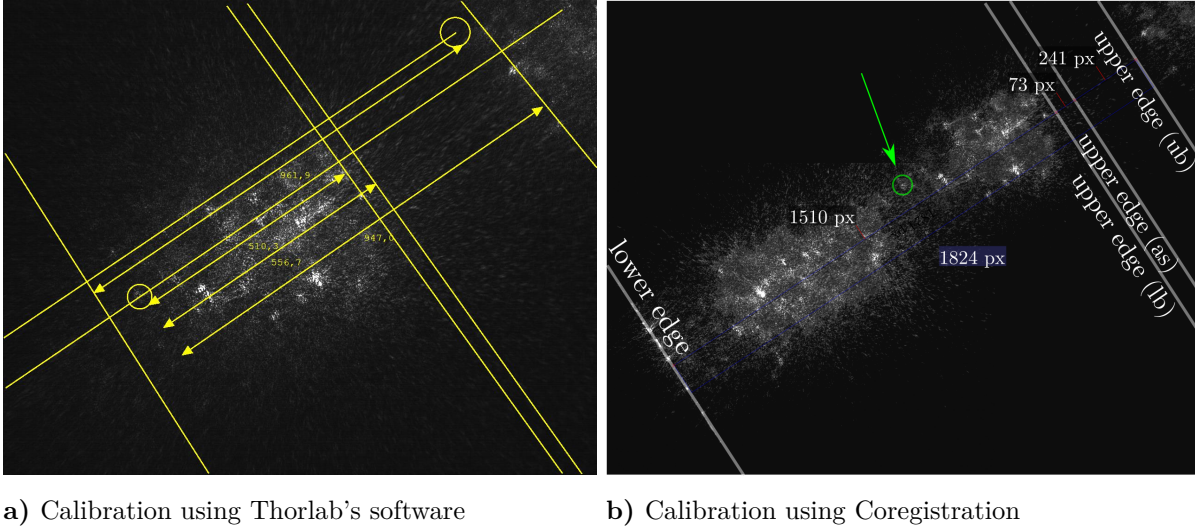
Figure 3.5: Calibration of the microscope imaging the microstrip (width $w_{\mathrm{MS}} = (1.00 \pm 0.25)\,\mathrm{mm}$). Resulting values are shown in Table 3.3. **(a)** Determination of the extend of the microstrip using Thorlab's software. The distance between upper and lower edge to a reference diamond are added to measure the width of the microstrip. **(b)** Determination of the extend by coregistration of the two images. A diamond has been tracked (arrow and circle) while moving the camera. Using GIMP [13] the images were manually registered. Annotations were done using Inkscape [14]. The acronyms at the lower edge correspond to *lower bound* (lb), *assumption* (as), i.e. the final value, and *upper bound* (ub), corresponding to the microstrip's shadow. The bluely-shaded value of 1824 pixels correspond to the distance between the lower edge and the upper bound of the upper edge. Blackly-shadowed numbers correspond to the line-to-line distances.

Table 3.3: Results of the microscope's calibration, in milli meters and pixels (px) for each determination type. The software rows correspond to the on-the-fly determination using Thorlab's in-house software (Figure 3.5a), coregistration to the manual coregistration of both images (Figure 3.5b), and the reference values correspond to the theoretical and ruler-based considerations (Equation 23).

method	lower bound	value	upper bound
software	1472 px	1519 px	1909 px
	0.95 mm	0.98 mm	1.23 mm
coregistration	1510 px	1583 px	1824 px
	0.97 mm	1.02 mm	1.18 mm
reference	1164 px	1552 px	1940 px
	0.75 mm	1 mm	1.24 mm

3.3.4. Electronic Components

An important quantity for ODMR measurements is the amount of microwave power deployed into the microstrip and the diamonds. Here, not the absolute value is from importance, but the relative amount of power deployed depending on the frequency. Since we are not able to measure this quantity directly in the current setup, the microstrip's transmission T_{MS} and reflection R_{MS} need to be determined. Having both of these values, the ratio of deployed power P_{MS} can be calculated:

$$P_{\mathrm{MS}} = 1 - (T_{\mathrm{MS}} + R_{\mathrm{MS}}). \tag{24}$$

In a final step, a correction term can be multiplied onto the ODMR signal. This correction term should amplify values within frequency ranges having less microwave power, and suppress those values with higher power. On the other hand, values with the average microwave power should not be corrected, minimizing effects of error evolution. Hence, we definied the correction term as

$$c_{\mathrm{corr}} = \frac{1}{1 + P_{\mathrm{MS}} - \bar{P}_{\mathrm{MS}}} \tag{25}$$

where $\bar{P}_{\mathrm{MS}}$ is the average value of P_{MS}. The determination of T_{MS} and R_{MS} can be achieved using a power coupler, which is described in the following:

All elements were characterized in a specific network using the SA's tracking generator. For each alement, a signal s has been acquired at the SA's input. In the following, we denote acquired network signals by $s^{\mathrm{IO}}_{\mathrm{Element}}$, where IO refers to input and output ports. s further refers to the total networks signal, and t/r describe the elements actual quantities (transmission t and reflection r) in units of dBm. For example, the power splitters transmission from port s to port

a) Schematic of the Setup

b) Resulting attenuation
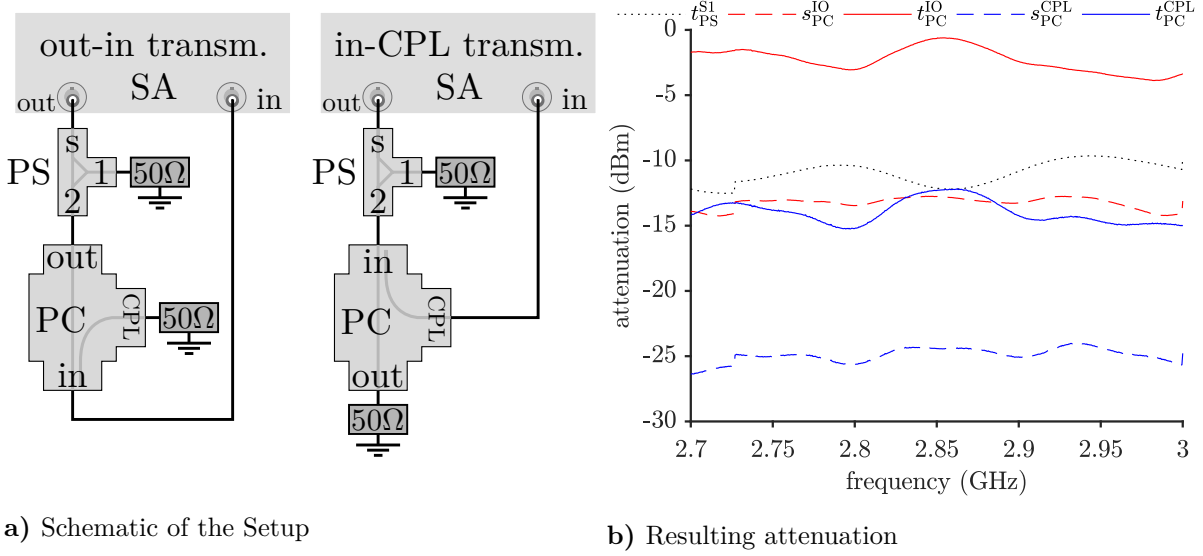
Figure 3.6: Calibration of the power splitter (PS) and power coupler (PC). **a)** Schematic of the setup. **SA** is the spectrum analyzer with its output and input port; **PS** is the power splitter; **PC** the power coupler; $50\,\Omega$ denote grounded impedances. **b)** Shown are the attenuations of the two elements of their respective ports: $t_{\mathrm{PS}}^{\mathrm{S2}}$ is the transmission of the power splitter from port S to port 1; $t_{\mathrm{PC}}^{\mathrm{OI}}$ is the transmission of the power coupler from output to input; $t_{\mathrm{PC}}^{\mathrm{CPL}}$ is the transmission of the power coupler from input to CPL; the respective s-quantities refer to the setups signal as shown in Figure 3.6a and explained in Equation 28.

1 is denoted by $t_{\mathrm{PS}}^{\mathrm{S1}}$. Furthermore, upper cases denote relative quantities and can be calculated by

$$T = \frac{10^{\frac{t}{10\mathrm{dBm}}}\,\mathrm{mV}}{1\mathrm{mV}}. \tag{26}$$

since the tracking generators reference lies at $1\,\mathrm{dBm}$.

As any kind of distortion in the final setup is important, the networks were set up similarly to Figure 3.1. To do som we firstly analyzed the transmissions $t_{\mathrm{PS}}^{\mathrm{S1}} = s_{\mathrm{PS}}^{\mathrm{S1}} = t_{\mathrm{PS}}^{\mathrm{S2}}$ by connecting the respective ports to the SA. As a next step, we analyzed the power coupler using the networks shown in Figure 3.6a. An important fact to keep in mind is that all unused ports need to be impedance matched and grounded, such that no reflections occur. The resulting transmissions $t_{\mathrm{PC}}^{\mathrm{OI}}$ from output to input and $t_{\mathrm{PC}}^{\mathrm{CPL}}$ from input to CPL were calculated according to

$$t_{\mathrm{PC}}^{\mathrm{OI}} = s_{\mathrm{PC}}^{\mathrm{OI}} - t_{\mathrm{PS}}^{\mathrm{S1}} \tag{27}$$

$$t_{\mathrm{PC}}^{\mathrm{CPL}} = s_{\mathrm{PC}}^{\mathrm{OI}} - t_{\mathrm{PS}}^{\mathrm{S1}}. \tag{28}$$

as a division in relative units corresponds to a subtraction in dBm.

a) Schematic of the Setup

b) Resulting attenuation
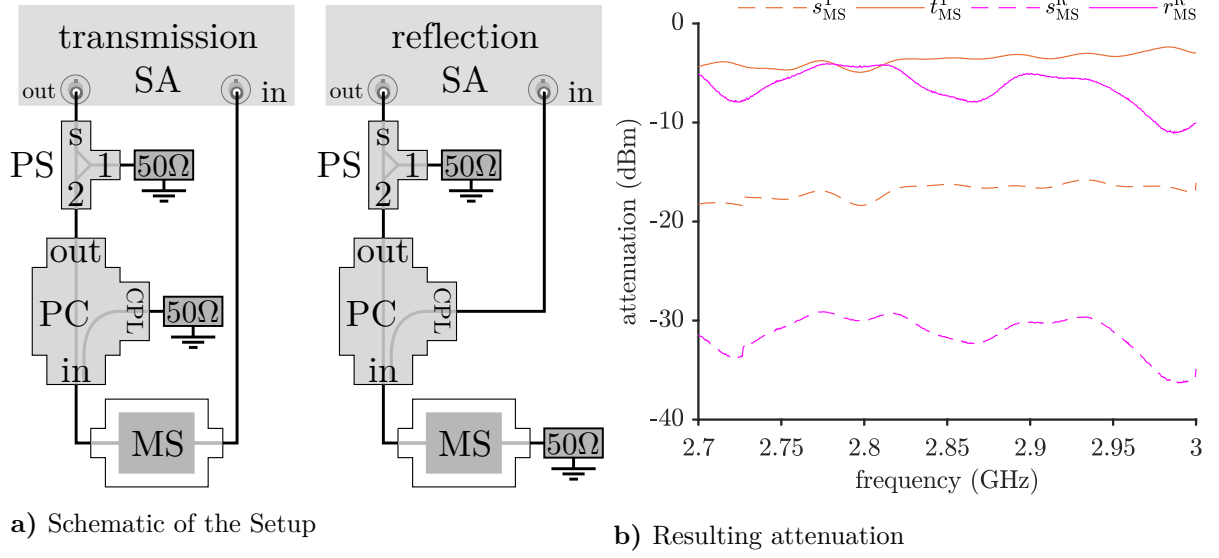
Figure 3.7: Calibration of the microstrip. **a)** Schematic of the setup. **SA** is the spectrum analyzer with its output and input port; **PS** is the power splitter; **PC** the power coupler; $50\,\Omega$ denote grounded impedances and **MS** the microstrip. **b)** Shown are the transmission t_{MS} and reflection r_{MS} of the microstrip, together with the respective network signal s. Both quantities are connected via Equation 29 and Equation 30, respectively. The attenuation of the PS and PC are presented in Figure 3.6.
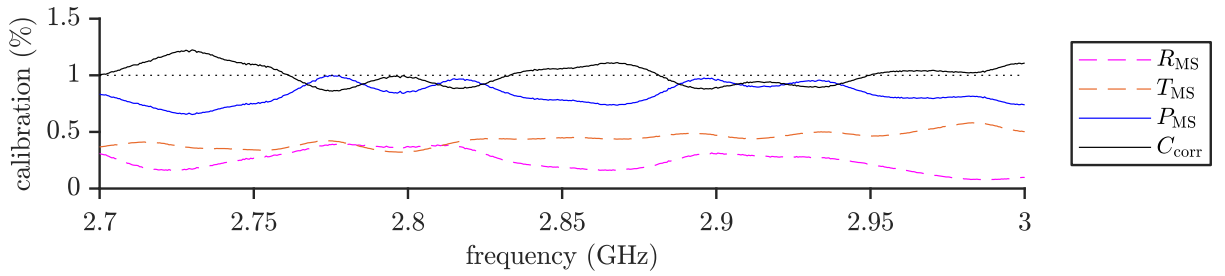
Figure 3.8: Results of the electronic calibration. Shown are relative transmission T_{MS} and relative reflection R_{MS}, as well as the ratio of deployed power P_{MS} (Equation 24) and the correction factor c_{corr} (Equation 25), which will later be multiplied onto the acquired ODMR signals.

While the transmission of the microstrip is acquired in a similar way to the previously described element, its reflection makes use of the power coupler: by connecting the PC input to the microstrip, its reflection can be observed at the CPL port. Both transmission and reflection setups are shown in Figure 3.7a, where

$$t_{\mathrm{MS}} = s_{\mathrm{MS}}^T - (t_{\mathrm{PS}}^{\mathrm{S1}} + t_{\mathrm{OC}}^{\mathrm{OI}}) \tag{29}$$

$$r_{\mathrm{MS}} = s_{\mathrm{MS}}^R - (t_{\mathrm{PS}}^{\mathrm{S1}} + t_{\mathrm{OC}}^{\mathrm{CPL}}) \tag{30}$$

are the respective calculations.

The resulting relative transmission T_{MS} and relative reflection R_{MS} , as well as the ratio of deployed power P_{MS} (Equation 24) and the correction factor c_{corr} (Equation 25) are shown in Figure 3.8 and will be used in the ODMR analysis.

3.3.5. APD Calibration

As mentioned in Section 3.2.3, the fluorescence signal was optimized using the laser in pulsed-mode. Since the laser is fully switched on and off, the difference between minimal and maximal amplitude corresponds to the highest possible contrast. It can therefore be used as a normalization coefficient for the ODMR measurements, which can then be reported in percent of maximal contrast. For an automated and reproducible calibration, the function peakdet[2] of MATLAB (version 2017a, Mathworks, Natick, USA) has been used. The calibration value was subsequently determined by subtracting the minimum value of the recorded signal from the maxima's mean. An exemplary calibration trace is shown in Figure 3.9.
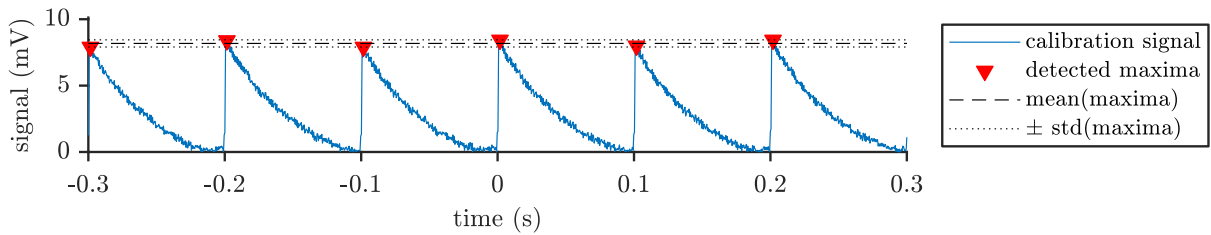
Figure 3.9: Exemplary, optimized APD signal (pulsed laser mode) used for optical contrast calibration. Using a peak detection algorithm with minimal prominence, the mean value of all peaks (denoted by red triangles) was used as a calibration factor for the following ODMR measurements.

---

[2]Paramters: The minimal peak prominence has been set to half of the maximal amplitude, showing reliable detection for all calibration signals.

3.3.6. Magnetic Field

In order to quantify the magnetic field at the microstrip, all four orientations of the magnets in the plastic jig have been measured. Further, the influence of the orientation of the magnets (south and north) has been measured by repeating the measurements with reverse magnet orientation. This results into magnetic fields strengths in the respective direction of $B_{0,x} = (3.1 \pm 0.1)\,\mathrm{mT}$, $B_{0,y} = (3.1 \pm 0.1)\,\mathrm{mT}$ and $B_{0,z} = (3.6 \pm 0.1)\,\mathrm{mT}$.

To allow the magnetic field to be observed throughout the ODMR measurements, a modified version of the plastic jig has been printed with the 3D printer. Further, a metal mount has been manufactured in the available workshop to keep the gauge in a constant position.

3.4. Methods

In general, all ODMR measurements were acquired $N = 200$ times. The values displayed in the upcoming chapters are the mean values over all N measurements, and their error bars correspond to their standard error.

3.4.1. Time-to-Frequency Conversion

During the course of the experiment, it became evident that the tracking generator's reaction did not follow immediately on the trigger by the signal generator. Hence, a simultaneous acquisition of the tracking generator was necessary. As an additional feature, we therefore included the power splitter together with the power detector, whose output has also been recorded by the oscilloscope.

One exemplary measurement of two channels (power detector, ODMR signal) is shown in Figure 3.10. As one can see, a clear point where the acquisition starts is not visible in the power detector's trace.[3] On the other side there is a well defined point (at around 220 ms) where the tracking generator is turned off. The transfer from the oscilloscope's time to the tracking generators frequency has been achieved by following the upcoming steps, where t_{sweep} is the tracking generators sweep time, f_c is the center frequency and f_{span} the frequency span:

1. Detect the turn-off point t_{end}: The maximum of the derivative of $|s_{\mathrm{PD}}(t)|$ at $t > t_{\mathrm{sweep}}$ corresponds to t_{end}. The starting point t_{start} can be calculated using the relation $t_{\mathrm{start}} = t_{\mathrm{end}} - t_{\mathrm{sweep}}$.
2. Cut out the time interval $[t_{\mathrm{start}}, t_{\mathrm{end}}] = I$.
3. Distribute the frequency onto each time point of I in the range of $[f_c - f_{\mathrm{span}}, f_c + f_{\mathrm{span}}]$.

---

[3]Note that the step function at 50 ms is due to an internal range change in the SA.

This process method yielded a reliable algorithm, although the internal processes of the spectrum analyzers remain not completely clear. Particularly the step in power at around 50 ms should be avoided in future measurements. If in the subsequent analysis steps obvious asymmetries were observed, we shifted the frequency offset to up to 15 MHz, as we reasoned that the spectrum analyzer's output did not perform linear steps when sweeping the frequency.

### 3.4.2. Background Correction and Gaussian Fitting

To determine the position of the observed resonances, we performed weighted linear least-squares fitting. As we assumed the NV centers' resonances to be normally distributed around their 'actual' frequency, we used a GAUSSIAN as a reference function. Yet, the signal needs to be flattened, as the different amplification steps do not allow the application of a GAUSSIAN. To do so, a third order polynomial function was subtracted, taking only values greater than 0.95 of the minimum into account.

As a second step, we performed least-squares GAUSSIAN fitting. By counting the signal's dips, we manually determined the number of resonances. Afterwards, a sum of GAUSSIAN functions has been modeled to fit the signal. If necessary, the range of the fit parameters was manually determined. The overall process is shown in Figure 3.11.

3.4.3. CCD-ODMR Analysis

As described in physical concepts section 2.1, the application of a microwave signal on the microstrip leads to a temporary decrease in brightness of the absorbed spectrum. Therefore, by sweeping through the resonance frequency in a constant period, the measured intensity in the CCD should decrease. To validate this theoretical thought, multiple CCD images have been recorded with and without the microwave signal. In greater detail, a series of images has been recorded with a microwave signal that was switched off after 20 seconds.

To quantify the brightness, the mean value over all pixels has been calculated for each CCD image. To minimize the distortion of background effects, the analysed area has been tailored to the extend of the diamond.
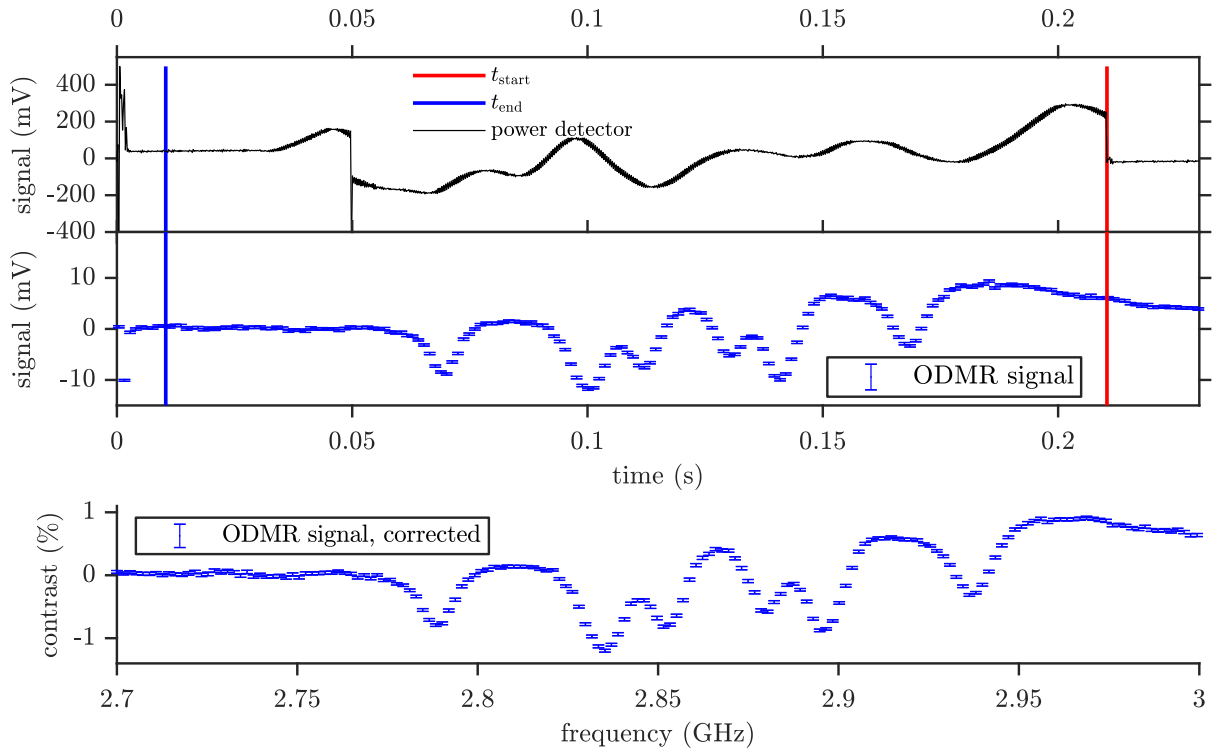
Figure 3.10: Time to frequency conversion by means of an exemplary ODMR measurement. **Top:** Signal of the power detector. The detected turn-off and calculated starting point (Section 3.4.1) are denoted by a red and blue line, respectively. **Middle:** Corresponding ODMR signal. **Bottom:** ODMR signal in the frequency domain after the correction factor (Section 3.1.2) was applied.
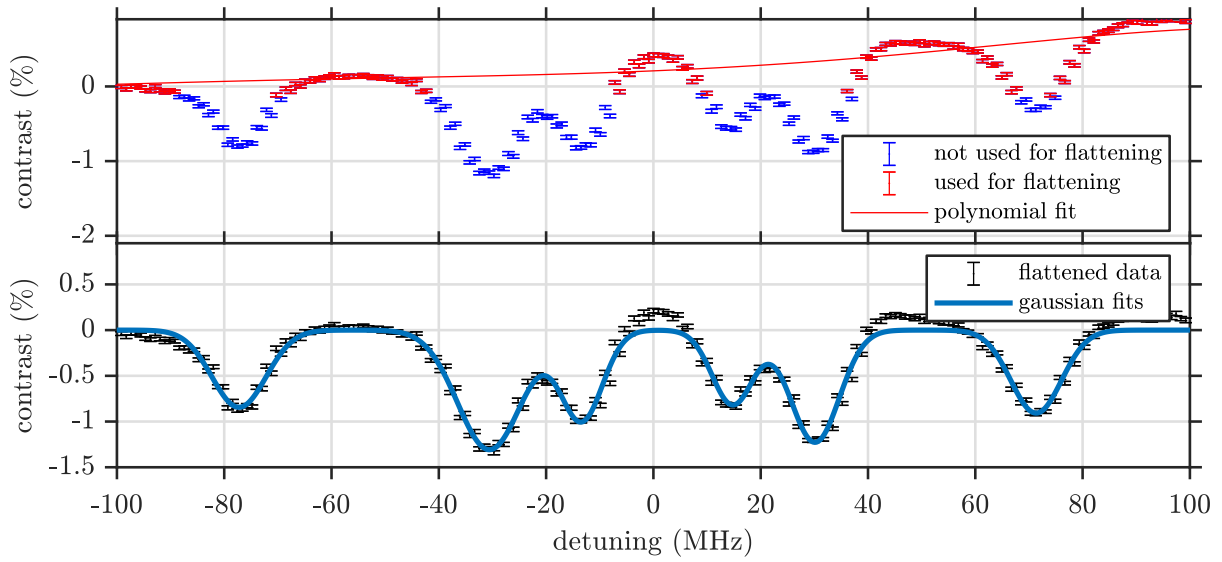
Figure 3.11: Visualization of the post-processing steps by means of an exemplary ODMR measurement. **Top:** Flattening process. Shown is the corrected signal (Section 3.1.2), where red points indicate those used for flattening. A polynomial fit of third order was performed to flatten the data in a reasonable manner. **Bottom:** Flattened data with 6 GAUSSIAN fits to determine the respective resonances.

4. Results

4.1. Size of the Diamonds

To determine the maximal lateral extent of the diamond, we retrieved line scans from the CCD images. Afterwards, the conversion factor (Section 3.3.3) was used to obtain the actual dimensions. To quantitatively deduct the lateral dimension, we took the height profile's derivate $h'_{\mathrm{l/r}}$ and detected its maxima (left and right). The corresponding FWHM (full width, half maximum) of the derivatives were used as an error margin. The images of the respective line scans of the two scanned diamonds are shown in Figure 4.1. The determined lateral extents are denoted in Table 4.1. Diamond 1 appeared to have equal edge widths, which is reflected in the

Table 4.1: Determined lateral dimensions of the diamonds. The corresponding line scans are shown in Figure 4.1.

	Line Scan 1	Line Scan 2
Diamond 1	$(20 \pm 12)\,\mu m$	$(20 \pm 11)\,\mu m$
Diamond 2	$(30 \pm 9)\,\mu m$	$(15 \pm 12)\,\mu m$

lateral extent of both line scans with $(20 \pm 11)\,\mu m$. Nevertheless the error margins are in the range of 50 % , which was expected (Section 3.3.3). Diamond 2 on the other hand appeared to have an elongated shape, which can also be verified by the difference in lateral size $((30 \pm 9)\,\mu m$ versus $(15 \pm 12)\,\mu m)$. There might be the possibility though that we observe two diamonds simultaneously, which would explain the factor of 2 between the two line scans.

4.2. Fluorescence Spectrum and NV Centre Identification

Figure 4.2 shows the fluorescence spectrum of diamond 2 with a dashed line indicating the expected position of the zero phonon line ($\lambda_{\mathrm{ZPL}} = (643 \pm 2)\,\mathrm{nm}$). The fluorescence spectrum of diamond 1 reproduces this result consistently. Therefore, this has been taken as evidence for the zero phonon line arising from the negatively charged NV^- center. The expected drop in intensity due to the long pass filter is slightly visible at $\lambda = 605\,\mathrm{nm}$. Besides that the phononic side bands are present, having an unexpected shoulder in the range of 770 to 810 nm.

4.3. ODMR-Results

### 4.3.1. Experiments without an External Magnetic Field

After isolating the single diamonds and identifying their zero phonon line, the application of a microwave signal did lead to a frequency dependent decrease in intensity. Figure 4.3 shows that

a) Image of diamond 1

b) Image of diamond 1

c) Line scans of diamond 1

d) Line scans of diamond 2
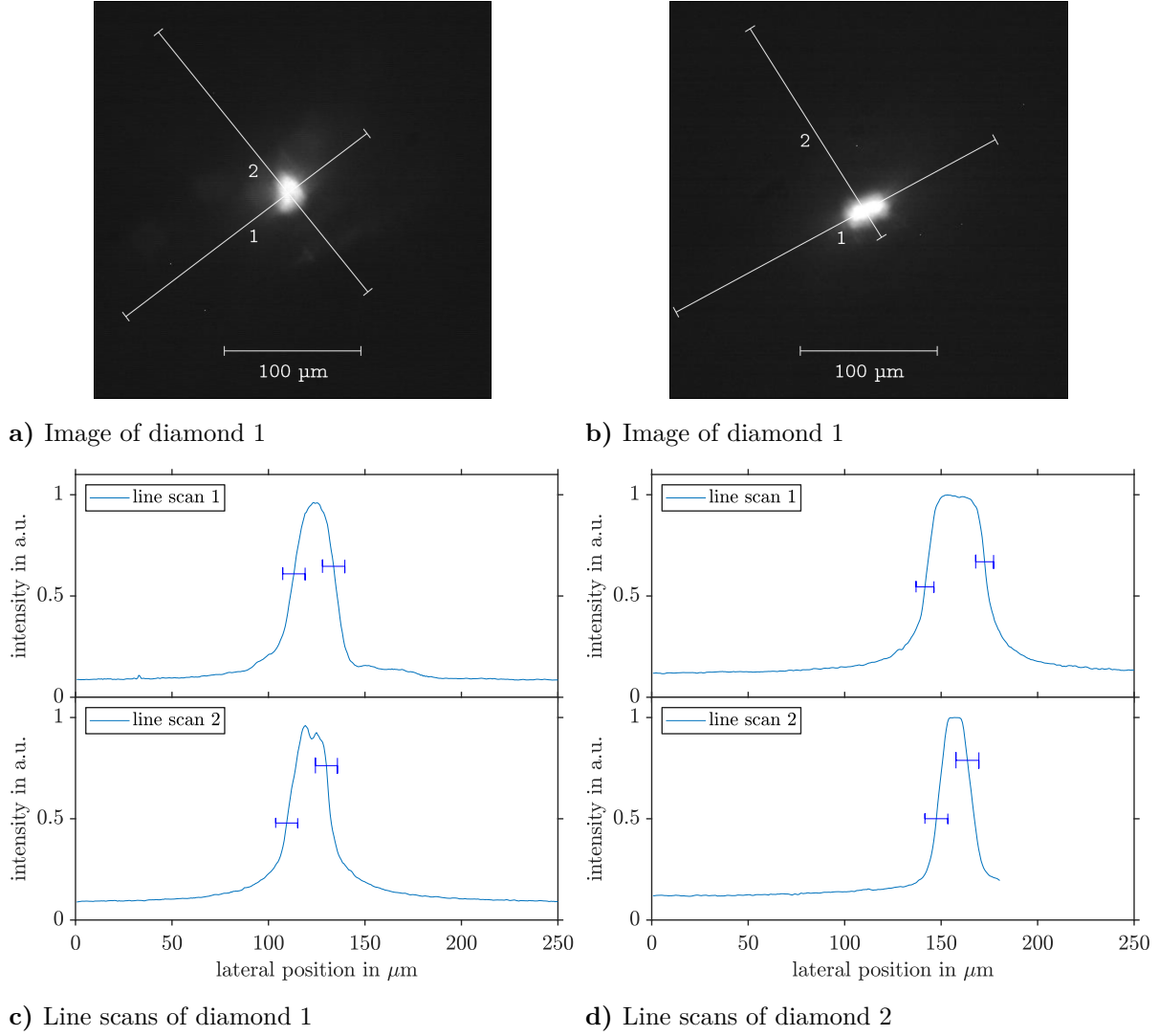
Figure 4.1: Determination of the lateral dimensions of the two scanned diamonds. **a) and b):** Respective CCD images. The annotated lines correspond to the line scans c) and d). **c) and d):** Line scans of the two diamonds. The detected edges are annotated by horizontal error bars. The determined distances are also shown in Table 4.1.
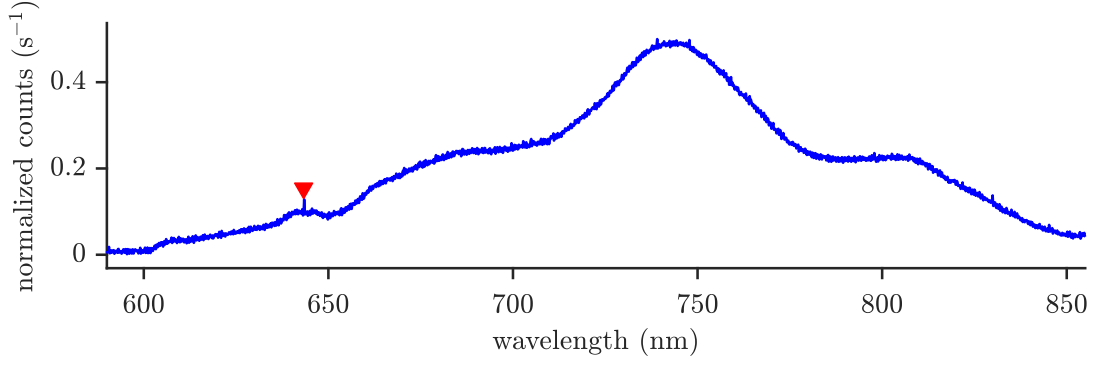
Figure 4.2: Fluourescence spectrum of diamond 2 with the zero phonon line indicated by a red triangle ($\lambda_{\mathrm{ZPL}} = (643 \pm 2)\,\mathrm{nm}$).
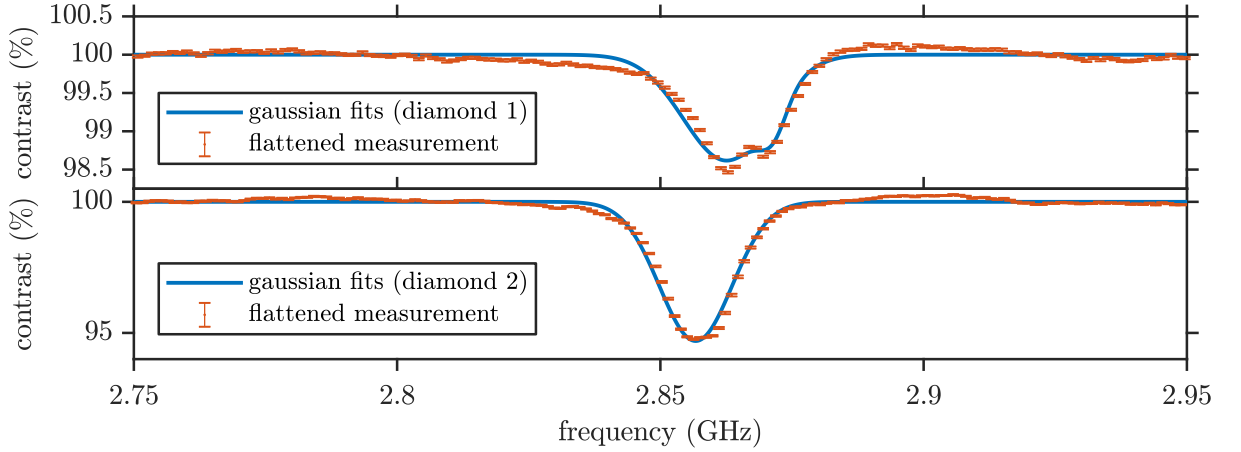
Figure 4.3: Results of the ODMR without an additional magnetic field in terms of the absolute frequency. **Top:** Results for diamond 1 with a split resonacne and a center frequency of $f_1^c = (2.87 \pm 0.01)\,\mathrm{GHz}$. **Bottom:** Results for diamond 2 with a single resonance and a center frequency of $f_2^c = (2.85 \pm 0.01)\,\mathrm{GHz}$. Note the difference in scale for both plots.

in the absence of a magnetic field, one 'dip' in intensity was measured while sweeping through the frequency spectrum. The fitted GAUSSIANS beared center frequencies of (2.87 ± 0.01) GHz and (2.85 ± 0.01) GHz for diamond 1 and diamond 2 respectively, yielding a mean observed resonance frequency of (2.86 ± 0.02) GHz. For the second diamond, the enhanced signal showed contrast values of to 4.8 %, which was 3 fold higher than the first measurements.

Whereas for the first diamond, a splitting in the dip is observed, the second one clearly shows a single dip. Since a manual analysis of the split resonance showed that they are only 8 MHz apart, the automatic detection was not able to distinguish both with the calculated error margins. The offset of 4 MHz towards a center frequency would yield a present magnetic field of 103 µT, which can be compared to the earth magnetic field in the discussion.

4.3.2. Experiments with an External Magnetic Field

Figure 4.4 shows the optical contrast under the influence of a magnetic field recorded for diamond 1. Whereas for the uppermost plot the magnetic field is zero, the lower plots contribute to two perpendicular magnetic fields in the horizontal plane. These lower plots clearly show up to four dips, symmetrically disposed around the centre frequency of (2.87 ± 0.01) GHz. In x-direction, only three resonance pairs are observed, which hold higher contrasts, though, which can be a sign that multiple resonances overlap. With an magnetic field in y-direction, we observe a symmetric distribution of 4 resonance pairs over frequency, while not having symmetric amplitudes. Note that the drop in amplitude towards lower frequencies in y-direction is due to a badly conditioned polynomial fit.

Table 4.2: Results of the ODMR experiments with an external magnetic field for diamond 1 (appendix, Figure 4.4) and diamond 2 (Figure 4.5). Shown are the respective detected resonances, in falling order of detuning frequency. f_i ($i = x, y, z$) are the detected detuning frequencies. B_i denote the experienced magnetic field strength, calculated using Equation 14. $d_i/|\vec{d}|$ is the normalized direction, calculated according to Equation 19. * denote that the respective resonance was not measured.
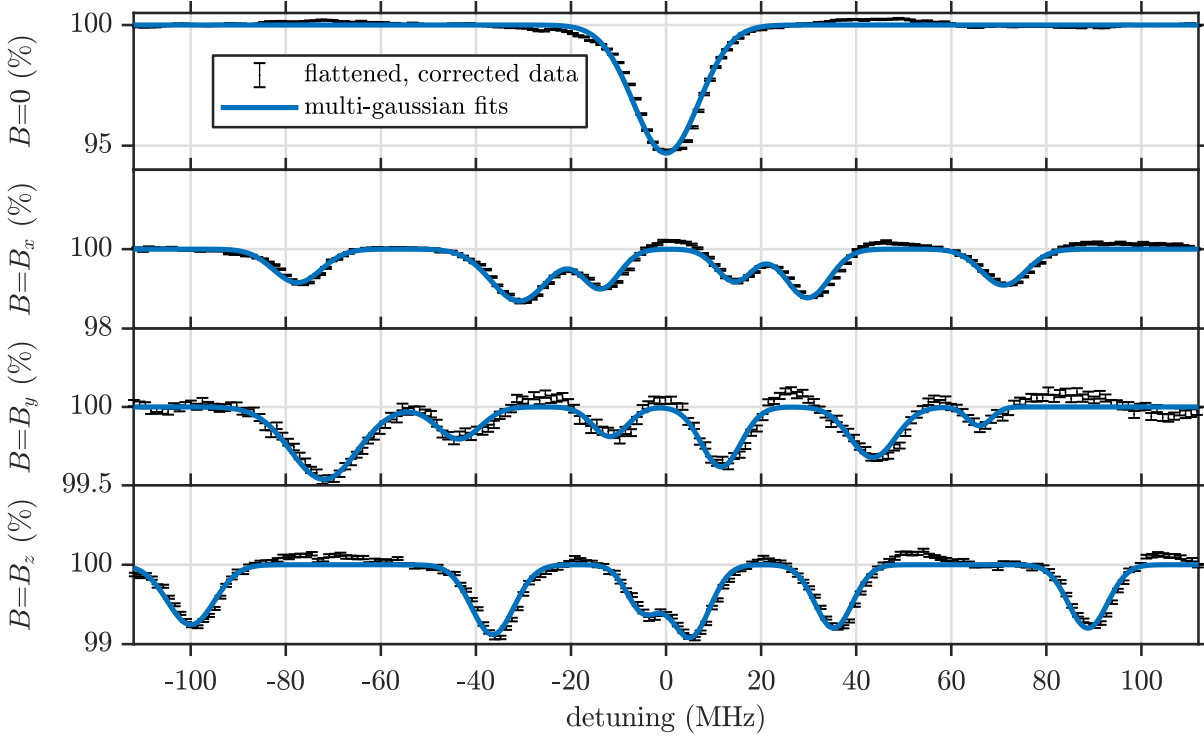
direction	diamond 1				diamond 2		
resonance	1	2	3	4	1	2	3
f_x (MHz)	70 ± 1	46 ± 3	22 ± 7	*	74 ± 7	30 ± 2	14 ± 1
f_y (MHz)	86 ± 14	51 ± 7	23 ± 5	11 ± 3	69 ± 8	44 ± 2	12 ± 2
f_z (MHz)	*	*	*	*	94 ± 13	36 ± 2	5 ± 4
B_x (mT)	2.51 ± 0.05	1.65 ± 0.12	0.77 ± 0.24	*	2.65 ± 0.26	1.08 ± 0.06	0.50 ± 0.05
B_y (mT)	3.07 ± 0.51	1.84 ± 0.26	0.84 ± 0.18	0.41 ± 0.12	2.46 ± 0.28	1.55 ± 0.06	0.42 ± 0.06
B_z (mT)	*	*	*	*	3.37 ± 0.45	1.28 ± 0.09	0.18 ± 0.13
$d_x/|\vec{d}|$	0.81 ± 0.25	0.53 ± 0.17	0.25 ± 0.11	*	0.86 ± 0.28	0.35 ± 0.11	0.16 ± 0.05
$d_y/|\vec{d}|$	0.99 ± 0.35	0.59 ± 0.20	0.27 ± 0.10	0.13 ± 0.06	0.79 ± 0.26	0.50 ± 0.16	0.13 ± 0.05
$d_z/|\vec{d}|$	*	*	*	*	0.94 ± 0.36	0.36 ± 0.13	0.05 ± 0.04
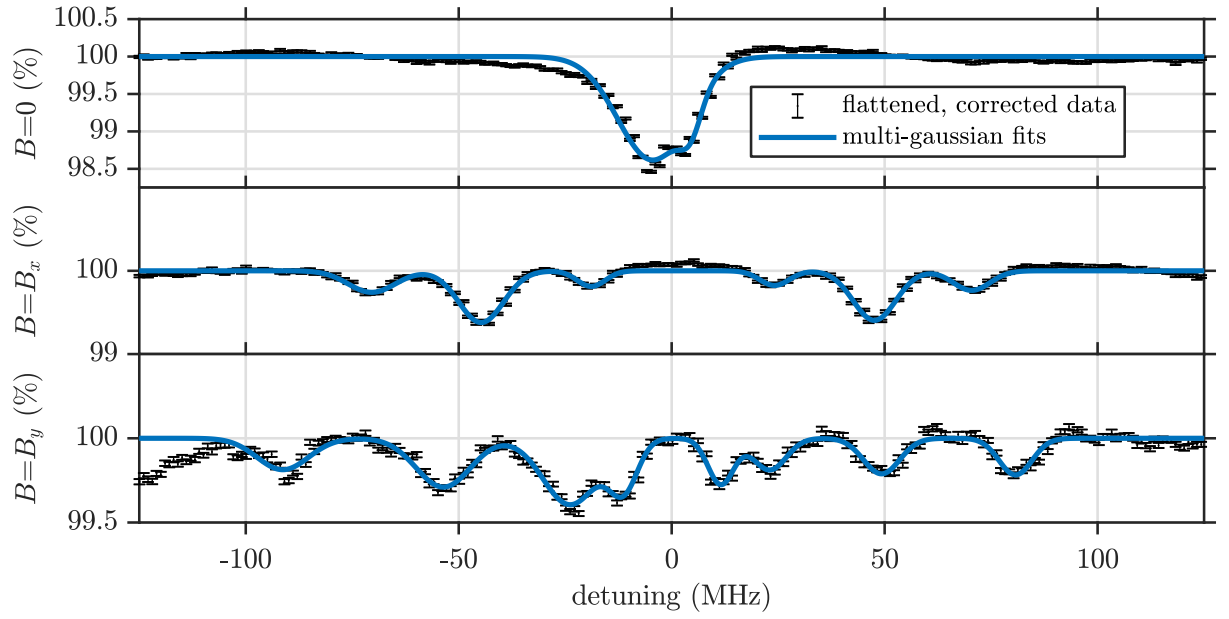
Figure 4.4: Results of the ODMR experiments at different magnetic field directions of diamond 1. The center frequency is (2.87 ± 0.01) GHz. Note that values are displayed as optical contrast (%) for the respective field and direction. The detected resonances f_x, experienced magnetic fields B_i and directions d_i are shown in Table 4.1. Note that the drop in amplitude towards lower frequencies in y direction is due to a badly conditioned polynomial fit.

Figure 4.5: Results of the ODMR experiments at different magnetic field directions of diamond 2. The center frequency is $(2.85 \pm 0.01)\,\text{GHz}$. Note that values are displayed as optical contrast (%) for the respective field and direction. The detected resonances f_x, experienced magnetic fields B_i and directions d_i are shown in Table 4.1.

For the second diamond, measurements for three perpendicular magnetic fields have been recorded and are shown in Figure 4.5. These also yield pairs of up to three resonances, centered at $(2.85 \pm 0.02)\,\text{GHz}$. In all directions, three resonance pairs were observed. Whilst the contrast amplitude is symmetric for the measurements with an magnetic field in x- and z-direction, we are again able to observe resonances with asymmetric in y-direction. Furthermore, higher detuning frequencies appear to not match their counterpart, e.g. the outermost frequency in z-direction with $f_{\text{left}} = (100 \pm 5)\,\text{MHz}$ and $f_{\text{right}} = (100 \pm 5)\,\text{MHz}$. When calculating the error margins for the determined frequency, we took this mismatch into account by adding half of the difference on top of the standard error. This way we ensure that all observed resonances are covered within the error margins of the determined values.

Table 4.1 summarizes the ODMR detuning from the center frequency for both diamonds and each magnetic orientation. Additionally to frequencies, the experienced magnetic field, calculated according to Equation 14, and the corresponding normalized NV center orientation are listed. As already stated, higher detuning frequencies result in increased error margins because

of the symmetry mismatch. One can also see that the experienced magnetic fields are lower than the maximum applied magnetic field strengths ($B_{0,x} = (3.1 \pm 0.1)\,\text{mT}$, $B_{0,y} = (3.1 \pm 0.1)\,\text{mT}$ and $B_{0,z} = (3.6 \pm 0.1)\,\text{mT}$, see Section 3.3.6). Hence, the normalized direction are never greater or equal than one, providing self-consistency in the data.

4.3.3. CCD-ODMR Analysis

As a check of consistency the ODMR measurement was performed with the CCD instead of the APD for diamond 2. Figure 4.6 shows the normalized intensity in arbitrary units against the time. After 20 seconds, an increase from $(66.3 \pm 0.1)\,\text{a\,u}$ to $(69.1 \pm 0.1)\,\text{a\,u}$ can be observed. This yields that the microwave signal reduces the signal intensity by $(4 \pm 1)\,\%$ which is in line with our previously presented APD results (Figure 4.3).
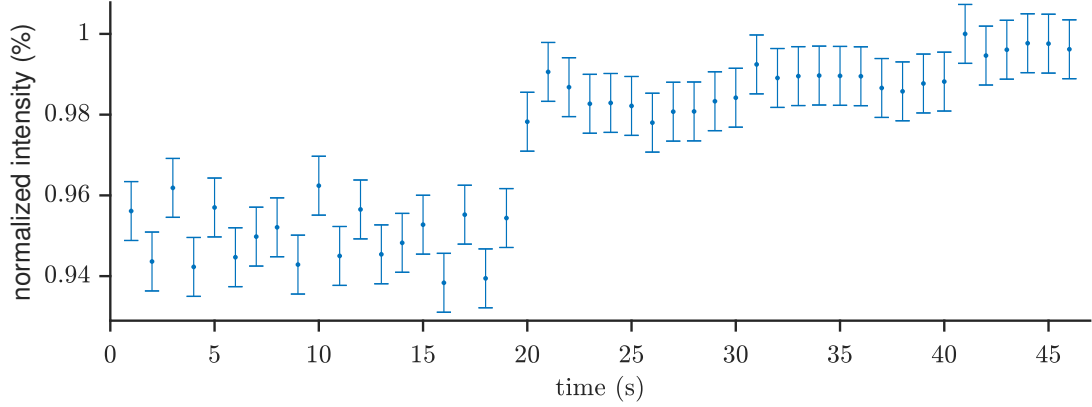
Figure 4.6: Mean value over all pixels calculated for each CCD image as a function of time (one image recorded per second). The microwave signal was initially present and then turned off after 20 seconds.

5. Discussion

5.1. Experiments

The determined sizes of the diamonds, ranging from 15 to 30 µm, were inline with those provided by the manufacturer (20-30 microns, *monocrystalline diamond powder*, 100 carats, MICRODIA-MANT, Langwil, Switzerland). In a future analysis, we might reduce the error margins by only taking the HWHM of the line scans' derivatives, which were generously engineered. To verify the accuracy, further calibrations of the microscope need to confirm our assumptions, though.

After identifying the fluorescence to be from an NV^- center, we continued to perform frequency resolved ODMR-experiments. Without an external magnetic field, we observed the degenerated resonances at (2.86 ± 0.02) GHz, which is inline with the expected value of 2.87 GHz [4, p.90] for both diamonds within uncertainties. The split resonance of diamond 1 may be due to the earth magnetic field, although the obtained values are on the order of three too high when taking the literature value ($B_{earth}^{max} = 44$ µT in middle Europe). Due to the fact that they are barely distinguishable, the relation holds within uncertainties. The detected contrast were consistent with the CCD-ODMR-measurements.

With an external magnetic field, we were able to detect up to four magnetic resonances, corresponding to the four orientations of the NV^- center. All of them had a spatial dependency on the magnetic field. Furthermore, the calculated experienced magnetic fields B_i were always lower than the measured, external magnetic field, providing consistency. Afterwards, the theoretical, normalized orientations for each detected resonance were calculated. Due to their relative error from 25 % to up to 50 %, a determination of the actual orientation in the laboratory frame was not performed in this experiment.

An unexpected point was the asymmetry of the optical contrast in amplitude. Even with the correction factor applied, positive contrasts were obtained at higher frequencies. It is unlikely that this is actually a physical phenomena. A reasonable explanation could be that the directions of the NV centers are not equally distributed. Further degrees of freedom within the experiment (e.g. magnetic field inhomogeneities) might further influence this asymmetries. It could also be that the spectrum analyzer behaves in a way which is not reflected in the calibration, which is discussed in the next section.

5.2. Calibration

The calibration steps were not only an important part of the analysis, but also facilitated the conduction of the experiment. The familiarity with the single components helped to optimize the optical signals and process the obtained data.

Besides that, we think that the calibration of the microscope and the APD were crucial for the analysis, as they confirmed that the in-house built setup is working correctly. On the other side, the calibration of the optical spectrometer was in our opinion too time consuming to detect an offset of a few nanometers. This uncertainty is smaller than the one of the line widths. We recommend to leave this calibration step to the very end, if time is still available.

The calibration of the electronic components on the other hand was very important to understand the setup and should definitely be performed. Due to the previously noted unknown internal behavior of the spectrum analyzer, the interpretability of this calibration bears some difficulties. One point, for example, is that Equation 30 should actually include the transmission term of the power coupler, i.e.

$$r_{\mathrm{MS}} = s_{\mathrm{MS}}^{R} - (t_{\mathrm{PS}}^{\mathrm{S1}} + t_{\mathrm{OC}}^{\mathrm{CPL}} + t_{\mathrm{OC}}^{\mathrm{OI}}) \tag{31}$$

which yielded values which are physically not possible (i.e. $T + R > 1$). This is consistent with previous results, which is why we removed the term for the sake of this experiment.

As already discussed in the methods, the time-to-frequency conversion lacks some reliability due to the internal processes of the spectrum analyzer. This can be partially avoided by obtaining the power detector's signal in advance and choosing a frequency range without a step function. Furthermore, the behavior of the spectrum analyzer should be further analyzed, or a different microwave generator should be used. We would further question the linearity of the tracking generator's frequency sweep, as some time offsets needed to be manually adjusted, preserving the signal's symmetry regarding frequency.

5.3. Outlook

One of the main achievements which remains undone in this report is the determination of the NV^- centers' orientations in the laboratory frame. To do so, two options are possible: One can either improve the uncertainty of the determined references to a point such that Equation 20 holds, and then sort the observed resonances manually. A problem could be though that two orientations fall on the same resonance, and can thus not be distinguished. As another option, one could mount the diamond on a rotating stage, and align it such that the resonance observed is at its maximum. In this case, the magnetic field and NV orientation are aligned; the other orientations can be calculated using the tetrahedral structure of the diamond. A problem for both methods is that one cannot differentiate if the magnetic field is parallel or antiparallel.

The experimental setup could be further improved such that the CCD, APD and spectrometer can be used simultaneously. Using only one lens (f_2) generally provided robustness of the setup, but made a simultaneous focussing on CCD and APD impossible. Having a lens for each

optical component could solve that problem.

Lastly, the determination of the shape of the diamond could not be performed in a sophisticated manner. For this point, we recommend to not use a reflective, rough microstrip for microscopy, where stray light is a dominating factor worsening the PSF. Instead, a professional microscope should be used.

5.4. Conclusions

We were able to perform a decent set of calibration measurements which were mostly applied in the subsequent analysis. Further adjustments in the setup did improve the optical contrast by a factor of 5 and also enabled the application of magnetic fields in vertical direction. After identifying the NV^--center in the fluorescence spectrum, it was possible to optically detect the magnetic resonance of the triplet state without an magnetic field. After applying a controlled, external magnetic field, the previously degenerated levels could also be distinguished.

In the end, this experiment provided an excellent opportunity to perform ODMR experiments while applying knowledge in magnetic resonance-, atomic-, solid-state- and quantum physics. We thus recommend the experiment to students on master level who would like to get an insight in state-of-the-art sensing technology.

Appendices

A. Supplementary Material

Table A.1: List of the used devices. 'Abbr.' denote the used abbreviations in the corresponding setups, shown in Figure 3.1, Figure 3.6a and Figure 3.7a. Adapted from [7], extended.

category	device	abbr.	vendor	part no
optical	laser	laser	Toptica	IBEAM-SMART-515-S
	CCD spectrometer	OS	Thorlabs	CCS175/M
	CMOS camera	CCD	Thorlabs	DCC1545M
	avalanche photo diode	APD	Thorlabs	APD430A2/M
	spheric lens	$f_{1/2}$	Thorlabs	
	plano-convex lens	f_c	Thorlabs	
	dichroic mirror (90:10)	DC_1	Thorlabs	
	dichroic mirror (50:50)	DC_2	Thorlabs	
	optical long-pass filter	CF	Thorlabs	FELH0600
	Optical band-pass filter	CF	Thorlabs	
	power meter	-	Thorlabs	
electronic	spectrum analyzer	SA	Rigol	DSA 1030
	oscilloscope	osc.	Rigol	
	microwave amplifier	A_1	Mini-Circuits	ZHL-16W-43-S+
	microwave coupler	PC	Mini-Circuits	ZADC-10-63-S+
	power detector	PD	Mini-Circuits	ZX47-60-S+
	power splitter	PS	Mini-Circuits	ZFRSC-42-S+
	attenuator	-	Mini-Circuits	BW-N30W50+
	audio amplifier	A_2	IMG	Stage Line STA-2200 PA

B. Feedback

In our opinion, this experiment fits very well into the schedule of the Applied Physics Laboratory. We particularly enjoyed the following points

1. **Responsibility:** It was like being a group member: the conduction of the experiment was solely our responsibility, or at least it felt like it was. It was possible to modify the setup, include our own ideas, expand the acquisition code, just to name a few examples. Although being time consuming, this opened a lot of fun, particularly in comparison to other experiments.

2. **Workshop Tasks:** Being able to modify the experiment with basically full access to the workshop did not only give us the opportunity to refresh our skills, but also to think about new parts, e.g. the magnet holders or optimizing the RF-cage.

3. **Improvements:** The possibility to include our own ideas and improvements into the setup was not only worth by itself (i.e. for an improved setup), but creates familiarity with the setup itself. We believe that this helped us to understand some of the important steps and parts of the experiment.

While having the majority of points on the upside, we think that there are still some rooms for improvement. This includes the written test at the beginning of the experiment, which might be an unnecessary pressure on the students; for future generations, the questions of this test will be available anyway. Therefore, we recommend to either not perform the test, or provide the questions in advance.

Another point is the excessive calibration part. As noted in the discussion, we would recommend to leave some parts out. This can still be the students' decision, but help may be provided in a form of a calibration list sorted by importance.

Crucial problems are caused by the internal processes of the spectrum analyzer. We were not able to come up with a clear 'what to do', but some kind of readjustment should be done here, which might be a cross-validation with another spectrum analyzer (to see whether the frequency is distributed linearly over time). This measurement could be used as another calibration.

A helpful add-on for the introductory script would be a chapter about the microwave components used. Since control and RF-technology are not mandatory parts of the physics course, a hint where to look things up might help students to be well prepared. If possible, it would further improve the didactic value of the experiment if it would be split up in the following order

1. Theory-Session. On an afternoon before the experiment, the theory Q&A could be performed. This way, no time is lost on the first day of the experiment, and students who are not prepared get the chance to perform further reading (over the weekend).

2. Calibration-Session: Optics. On day one, the first part should be about the optical part of the experiment. We would not recommend to go directly into the electronic components as well, but save this for the afternoon. In this manner, not too much input is provided at one time.

3. Calibration-Session: Electrons. On day one (afternoon) or day two (morning), the second part about the electronics could take place.

4. Preliminary measurements: As soon as the optical signal is found, some preliminary ODMR measurements should be performed. This way, day 3 and 4 can be used to obtain improved results.

5. Result Enhancement: On the last two days, things which remained unclear thus far can

be redone and improved.

Please also note that not only the experiment is time consuming, but moreover the calibration and analysis. If all points are tackled, only the evaluation of the calibration can be quite excessive. In our case, only this part took about 15 working hours, not including the concepts and results. As the applied lab experiments usually have a submission deadline of two weeks, we recommend at least four weeks of data evaluation for this experiment.

To conclude, we would like to point out that the tutor's assistance and help was a big deal of the experiment being successful and fun. Particularly the 'friday-morning theory session' in advance helped us a lot.

List of Figures

List of Tables

References

[1] Vadym N Mochalin, Olga Shenderova, Dean Ho, and Yury Gogotsi. The properties and applications of nanodiamonds. *Nature Nanotechnology*, 7(1):11–23, 2011. ISSN 1748-3387. doi: 10.1038/nnano.2011.209. URL http://dx.doi.org/10.1038/nnano.2011.209. 1

[2] Marcus W. Doherty, Neil B. Manson, Paul Delaney, Fedor Jelezko, Jörg Wrachtrup, and Lloyd C.L. Hollenberg. The nitrogen-vacancy colour centre in diamond. *Physics Reports*, 528(1):1–45, 2013. ISSN 03701573. doi: 10.1016/j.physrep.2013.02.001. URL http://dx.doi.org/10.1016/j.physrep.2013.02.001. 1, 4

[3] Linh My Pham. Color Centers in Diamond. *PhD thesis*, (May), 2013. 1, 3, 4

[4] Romana Schirhagl, Kevin Chang, Michael Loretz, and Christian L. Degen. Nitrogen-Vacancy Centers in Diamond: Nanoscale Sensors for Physics and Biology. *Annual Review of Physical Chemistry*, 65(1):83–105, 2014. ISSN 0066-426X. doi: 10.1146/annurev-physchem-040513-103659. URL http://www.annualreviews.org/doi/10.1146/annurev-physchem-040513-103659. 1, 3, 4, 33

[5] A Gruber, A Dra, C Tietz, L Fleury, J Wrachtrup, and C Von Borczyskowski. Scanning Confocal Optical Microscopy and Magnetic Resonance on Single Defect Centers. 276(June 1997):2012–2015, 2012. 1

[6] Christian Gerthsen and Dieter Meschede. *Physik*. Springer-Lehrbuch, Berlin, 23 edition, 2006. ISBN 9783540254218. URL http://www.gbv.de/dms/hebis-darmstadt/toc/130220213.pdf. 3, 5

[7] J.-P. Schröder, D. Palani, O. Orlov, T. Schaetz, and U. Warring. Diamonds for Sensing Applications. In *Master Laboratory Applied Physics*, pages 1–7. Albert-Ludwigs-Universität, Freiburg, 2018-04-04. 8, I

[8] Wikipedia. Erdmagnetfeld – Wikipedia, the free encyclopedia, 2018. [Online; accessed 14-May-2018]. 11

[9] Bernd-Uwe Runge. *Physikalisches Anfängerpraktikum*. Universität Konstanz, Konstanz, 1 edition, 2012. URL https://ap.physik.uni-konstanz.de/index.php?Itemid=19. 11

[10] Kenneth R Lang. *Astrophysical Formulae: Space, time, matter and cosmology*. Springer, 2013. 13

[11] Alexander Rohrbach. *Lectures on Optical Trapping and Particle Tracking*. Albert-Ludwigs-Universität, Department of Microsystem Engineering, Freiburg im Breisgau, 2017. 14

[12] Thorlabs Inc. 1/2-Inch Megapixel CMOS Digital Image Sensor. In *Specsheets*. Thorlabs

Inc., Newton, NJ, 2018. 15

[13] The GIMP Team. GIMP: GNU Image Manipulation Program, 2018. URL https://www.gimp.org. 15, 16

[14] Inkscape Project. Inkscape, 2018. URL https://inkscape.org. 15, 16